



## Combined TiO<sub>2</sub>/SiO<sub>2</sub> mesoporous photocatalysts with location and phase controllable TiO<sub>2</sub> nanoparticles

E. Beyers<sup>a,\*</sup>, E. Biermans<sup>b</sup>, S. Ribbens<sup>a</sup>, K. De Witte<sup>a</sup>, M. Mertens<sup>c</sup>, V. Meynen<sup>a,c</sup>, S. Bals<sup>b</sup>, G. Van Tendeloo<sup>b</sup>, E.F. Vansant<sup>a</sup>, P. Cool<sup>a</sup>

<sup>a</sup> Department of Chemistry, Laboratory of Adsorption and Catalysis, University of Antwerpen (UA), Universiteitsplein 1, B-2610 Wilrijk, Belgium

<sup>b</sup> Electron Microscopy for Materials Science, EMAT, University of Antwerpen (UA), Groenenborgerlaan 171, B-2020 Antwerpen, Belgium

<sup>c</sup> Flemish Institute for Technological Research, VITO, Boeretang 200, B-2400 Mol, Belgium

### ARTICLE INFO

#### Article history:

Received 10 July 2008

Received in revised form 10 October 2008

Accepted 18 October 2008

Available online 28 October 2008

#### Keywords:

Location

Crystalline phase

Mesoporous SiO<sub>2</sub> support

TiO<sub>2</sub> photocatalyst

### ABSTRACT

Combined TiO<sub>2</sub>/SiO<sub>2</sub> mesoporous materials were prepared by deposition of TiO<sub>2</sub> nanoparticles synthesised via the acid-catalysed sol–gel method. In the first synthesis step a titania solution is prepared, by dissolving titaniumtetraisopropoxide in nitric acid. The influences of the initial titaniumtetraisopropoxide concentration and the temperature of dissolving on the final structural properties were investigated. In the second step of the synthesis, the titania nanoparticles were deposited on a silica support. Here, the influence of the temperature during deposition was studied. The depositions were carried out on two different mesoporous silica supports, SBA-15 and MCF, leading to substantial differences in the catalytic and structural properties. The samples were analysed with N<sub>2</sub>-sorption, X-ray diffraction (XRD), electron probe microanalysis (EPMA) and transmission electron microscopy (TEM) to obtain structural information, determining the amount of titania, the crystal phase and the location of the titania particles on the mesoporous material (inside or outside the mesoporous channels). The structural differences of the support strongly determine the location of the nanoparticles and the subsequent photocatalytic activity towards the degradation of rhodamine 6G in aqueous solution under UV irradiation.

© 2008 Elsevier B.V. All rights reserved.

## 1. Introduction

TiO<sub>2</sub> is one of the most studied photocatalysts, because of its low cost, high photocatalytic activity and chemical/photocorrosion stability under reaction conditions [1]. TiO<sub>2</sub> can be used as heterogeneous photocatalyst for water or air purification [2–4]. For a heterogeneous catalyst it is important to have a high surface area, with a high number of reactive sites. Therefore researchers often use TiO<sub>2</sub> with small particle sizes, leading to a high surface area and photocatalytic activity. The industrial interest for this material is however limited, because it is difficult and expensive to separate the catalyst from the liquid or gas. Therefore, a lot of research is done to increase the surface area of the TiO<sub>2</sub> catalyst without decreasing the particle size in order to easily separate and reuse the photocatalyst. The scientific research in this field can be divided into two classes: (1) On one hand researchers attempt to make TiO<sub>2</sub> itself mesoporous, similarly to mesoporous silica

materials. Nevertheless, the high hydrolysis and condensation rates of Ti- precursors make it difficult to prepare mesoporous titania. When the high reactivity of the Ti-precursor is not tempered, synthesis will lead to ill-defined mesoporous structures. There are a lot of possibilities to control the reactivity of the precursor: working in non-aqueous solvents, using a complexed titania precursor or working in strong acidic medium [5–7]. A second problem in making TiO<sub>2</sub> mesoporous, is the phase transformation that could happen upon calcination, necessary to remove the surfactant. Therefore the mesostructured material should be stabilised before calcination: modification with NH<sub>3</sub>, NH<sub>4</sub>OH or NaOH can be executed to increase the thermal stability of the synthesised materials [8–11].

(2) On the other hand, a silica material can be activated with titania. The activation can be carried out immediately, during the formation of the silica material (in-situ activation). This way, combined TiO<sub>2</sub>/SiO<sub>2</sub> materials, like aerogels [12–18], films [19,20] and mesoporous materials (MCM-41, MCM-50 and SBA-15) [21–26] have already been prepared. Irrespective of the type of material, the reactivity of the Ti- and Si-precursor have to be adjusted to each other. Most of the times, the Si-precursor is

\* Corresponding author. Tel.: +32 3 820 23 68; fax: +32 3 820 23 74.

E-mail address: [evi.beyers@ua.ac.be](mailto:evi.beyers@ua.ac.be) (E. Beyers).

prehydrolysed, before the Ti-precursor is added. The reactivity of the Ti-precursor is tempered by adding extra organic complexators, like acetylacetone or a surfactant [12,13,19,20]. The hydrolysis of the Ti-precursor can also be adjusted by a careful pH-control. The pH can be controlled by using urea, which is decomposed upon temperature increase, resulting in an elevated pH [23,24]. Another method to adjust the reactivities of the precursors is by first preparing an inversed microemulsion of  $\text{TiO}_2$  particles, which are then used in the preparation of combined  $\text{TiO}_2/\text{SiO}_2$  materials like MCM-41, MCM-50 and SBA-15. Depending on the applied Ti-precursor, different crystalline  $\text{TiO}_2$  phases can be formed [22]. For in-situ synthesis methods, the anatase formation is influenced by the  $\text{SiO}_2$  content and the calcination temperature. Therefore, anatase is not always present, which implies that in some cases the materials are not suited as catalyst for photocatalytic degradation reactions [23,24,27].

A second way to produce  $\text{SiO}_2/\text{TiO}_2$  materials is to introduce  $\text{TiO}_2$  in a pre-synthesised silica support by applying post-synthesis methods. Here, the  $\text{SiO}_2$  support material is first prepared and then loaded with  $\text{TiO}_2$ . Commercial  $\text{SiO}_2$  [28,29],  $\beta$ -zeolite [30], clays [2,3,30,31],  $\text{SiO}_2$  spheres [32,33] and ordered  $\text{SiO}_2$  materials, like MCM-41 [1] and SBA-15 [1,34–39] have already been activated with  $\text{TiO}_2$ . The  $\text{TiO}_2$  loading can be varied ranging from 3 to 80 wt% [1,28,30]. Different post-modification methods have been described in literature to deposit crystalline  $\text{TiO}_2$  on different supports: acid-catalysed sol-gel method [29,30], chemical solution deposition [40], internal hydrolysis [40] or multistep deposition [37,38,41]. By post-modification of porous materials, titania can be situated at different places in the porous network: the particles can be inside or outside the porous channels, whereby possible blocking of the pores occurs [42]. Nevertheless, many studies are not so detailed. Some studies do not even determine the amount of effectively deposited  $\text{TiO}_2$  [1,34]. The discussion of the position of the  $\text{TiO}_2$  nanoparticles (in- or outside the mesoporous channels) is often lacking or interpretation of data is incomplete [1,34,36]. However it is important to know the position of the  $\text{TiO}_2$  nanoparticles towards applications. If the  $\text{TiO}_2$  photocatalyst will be incorporated in e.g. wall paper or textile for the goal of air purification such as elimination of indoor odours and pollutants, it is important that the  $\text{TiO}_2$  particles are located solely inside the mesoporous structure, so that the outer surface of the  $\text{TiO}_2$  particles remains inactive. This way, the degradation of the colour of the wall paper and textile upon illumination with UV-light is prevented. So, the wall paper or textile can be used as catalyst themselves, to degrade air components.

In this article two different  $\text{SiO}_2$  materials (SBA-15 and MCF) will be modified by post-synthesis deposition based on the acid-catalysed sol-gel method. The amount of Ti-precursor and the temperature at which the particles are formed and deposited will be varied. Special attention will be paid to the location of the  $\text{TiO}_2$  particles in the mesoporous structure and the influence of its location on the photocatalytic activity of the material. The importance of the type of support will be demonstrated.

## 2. Experimental

### 2.1. Synthesis

#### 2.1.1. Support

For the synthesis of the mesoporous  $\text{SiO}_2$  supports (SBA-15 and MCF), the triblock copolymer P123 ( $\text{EO}_{20}\text{PO}_{70}\text{EO}_{20}$ , Aldrich) was used as structure directing agent and tetraethyl orthosilicate (TEOS, 98%, Acros Organics) as silica source. SBA-15 was synthesized according to the procedure described earlier by Van Bavel et al. [43]. 4.0 g of Pluronic P123 was dissolved in 150 mL

1.6 M HCl. Subsequently, 9.14 mL of TEOS was added. The obtained suspension was stirred at 45 °C for 8 h and then aged at 80 °C for 15 h. Afterwards the solid product was filtered, washed with distilled water and dried.

The synthesis method of MCF was based on the method, reported by Schmidt-Winkel et al. [44]. 4.0 g of Pluronic P123 was dissolved in 150 mL 1.6 M HCl solution at 35–40 °C. Then, 46.7 mg  $\text{NH}_4\text{F}$  and 2 g 1,3,5-trimethylbenzene (mesitylene, 99% Acros) were added and vigorously stirred for 1 h. Subsequently, 9.14 mL of TEOS was added. After 20 h stirring at 35–40 °C, the slurry was transferred into an autoclave and aged at 100 °C for 24 h. The obtained precipitate was filtered, washed with distilled water and dried.

#### 2.1.2. Post-modification

Prior to modification of the supporting materials, the samples were calcined at 550 °C with a heating rate of 1 °C/min and an isothermal period of 6 h. The post-modification of these supporting materials is based on the acid-catalysed sol-gel method of Battacharyya et al. [30]. Different amounts of Ti-isopropoxide (TTIP) ( $\text{Ti}(\text{O}^i\text{Pr})_4$ , 97% Aldrich), ranging from 0.6 mL to 7.4 mL, were added gradually to 30 mL of an aqueous 1 M  $\text{HNO}_3$  solution under continuous stirring for 2.5 h. Subsequently, the colloidal solution was diluted with 50 mL of water and the pH was adjusted to 3 with 1 M NaOH. At pH 3, there is an electrostatic interaction between the positively charged  $\text{TiO}_2$  particles and the negatively charged  $\text{SiO}_2$  support. Then, 0.5 g of the supporting material (SBA-15 or MCF) was added and the mixture was stirred for 2 h at room temperature. The obtained catalyst was separated by centrifugation, washed with water and dried. Finally, it was calcined at 300 °C for 6 h, with a heating rate of 1 °C/min.

### 2.2. Characterisation

For all samples, the surface area and the porosity were determined by a Quantachrome Autosorb-1-MP automated gas adsorption system. Prior to  $\text{N}_2$ -sorption, all samples were degassed at 200 °C for 16 h. The  $\text{N}_2$ -sorption was carried out at liquid nitrogen temperature (−196 °C). The specific surface area was calculated using the Brunauer-Emmet-Teller (BET) method. The pore size distribution was determined from the adsorption branch using the Barret-Joyner-Halenda (BJH) model. The total amount of  $\text{N}_2$  adsorbed at  $p/p_0 = 0.95$  was used to estimate the total pore volume.

X-ray diffraction (XRD) measurements were carried out on a PANalytical X'Pert PRO MPD diffractometer using filtered  $\text{CuK}\alpha$  radiation. Measurements were done in the 2 $\theta$  mode using a bracket sample holder with a scanning speed of 0.04°/4 s continuous mode.

The titania loading was determined with electron probe microanalysis (EPMA). The measurements were carried out on a JEOL JXA-733 apparatus.

High angular annular dark field-scanning transmission electron microscopy (HAADF-STEM) images were recorded using a JEOL 3000 F operating at 300 kV.

### 2.3. Adsorption and catalysis

For all catalysts, the adsorption and catalytic activity were investigated. Therefore, the rhodamine 6G concentration (initial concentration 0.00004 M) was measured at distinct time intervals by means of UV-vis spectroscopy (thermo-electron evolution 500). 0.32 mg catalyst per mL dye solution was used in all experiments. For the adsorption and catalysis experiment, 50 mL resp. 25 mL dye solution with 16 mg resp. 8 mg of catalyst was used. The

adsorption–desorption equilibrium was determined by measuring the dye concentration during 100 min without UV illumination. The second order constant was calculated using the following equation [45], where  $q_e$  is the equilibrium adsorption capacity in  $\text{mg g}^{-1}$  and  $k_2$  is the second-order constant in  $\text{g mg}^{-1} \text{min}$ . These variables can be calculated from the slope and intercept respectively.

$$\frac{t}{q} = \frac{1}{k_2 q_e^2} + \frac{t}{q_e}$$

Prior to each catalytic test, the adsorption–desorption equilibrium was established. Afterwards the rhodamine 6G solution was irradiated with a 100 W Hg lamp (Sylvania Par 38). The concentration of the remaining rhodamine 6G was analyzed every 10 min during 1 h. The catalytic experimental setup consists of a plastic batch photoreactor with cylindrical shape (40 mL). The catalyst powder was maintained in suspension with the dye solution by a magnetic stirrer placed at the bottom of the vessel.

### 3. Results and discussion

Different parameters in the acid-catalysed sol–gel method and the deposition method were changed. For the formation of the nanoparticles, the initial TTIP amount and the formation temperature were varied. During the deposition of these preformed nanoparticles, the temperature was changed. All these changes were executed on both (SBA-15 and MCF) supports. The influence on the structural properties was investigated as well as the impact on the resulting catalytic activity of these materials. For each parameter, the effects for SBA-15 will be described first, followed by the differences between the modified SBA-15 and MCF materials.

#### 3.1. The initial TTIP amount

A first parameter that was changed in the synthesis method is the amount of TTIP dissolved in the  $\text{HNO}_3$  solution, ranging from 0.6 to 7.4 mL. The  $\text{N}_2$ -sorption isotherms of the activated SBA-15 materials are shown in Fig. 1 together with the initial SBA-15 support. The porous characteristics of the materials are summarized in Table 1. Both show that upon the increase of the initial TTIP amount, the surface area and total pore volume decrease as a result of the larger deposited amount of  $\text{TiO}_2$ . The  $\text{N}_2$ -sorption isotherms of all the combined  $\text{TiO}_2/\text{SiO}_2$  materials are very different from the original SBA-15 support, showing a two-step desorption curve. Such a two-step desorption curve was earlier described for PHTS (plugged hexagonal templated silica) materials. The appearance of

**Table 1**

Structural properties of the samples prepared with different TTIP amounts.

	$S_{\text{BET}}$ ( $\text{m}^2/\text{g}$ ) <sup>a</sup>	$V_p$ ( $\text{cm}^3/\text{g}$ ) <sup>b</sup>	$D_{\text{BJH}}$ (nm) <sup>c</sup>	wt% $\text{TiO}_2$ <sup>d</sup>
SBA-15	761	0.87	7.3	–
0.6 mL SBA-15	657	0.78	7.3	17
2 mL SBA-15	534	0.63	7.3	38
4 mL SBA-15	359	0.39	7.3	63
6 mL SBA-15	314	0.30	7.3	70
7.4 mL SBA-15	289	0.28	7.3	75
MCF	640	2.43	26	–
0.6 mL MCF	526	1.73	26	19
2 mL MCF	473	1.26	26	41
4 mL MCF	412	0.74	24	56
6 mL MCF	380	0.54	22	71
7.4 mL MCF	330	0.42	16	74

<sup>a</sup>  $S_{\text{BET}}$  is the specific surface area.

<sup>b</sup>  $V_p$  is the total pore volume.

<sup>c</sup>  $D_{\text{BJH}}$  is the pore diameter determined from the adsorption branch using the Barret–Joyner–Halende (BJH) model.

<sup>d</sup> Determined with EPMA.

such a two-step desorption is typical for the existence of nanoparticles inside the mesoporous channels of SBA-15, which narrow the mesopores in distinct places [46–49]. The first step of the desorption branch originates from the open SBA-15 pores, the second step (closing at  $p/p_0 = 0.42$ ) comes from the narrowed pores. For the combined  $\text{TiO}_2/\text{SiO}_2$  materials, the appearance of such a two-step desorption curve can be ascribed to the introduction of  $\text{TiO}_2$  nanoparticles inside the channels of SBA-15, narrowing these channels in distinct places. X-ray analysis shows that after calcination, the  $\text{TiO}_2$  nanoparticles are present as anatase (see supporting information). The size of the crystalline nanoparticles was determined by the Warren–Averbach method [50]. For all the materials, the anatase particle size is 4.5 nm. The actual particle size is a little bit larger, 4.8 nm, determined with TEM (see supporting information). This means that for all the TTIP concentrations, the anatase nanoparticles could enter the mesopores of SBA-15, which has a pore diameter of 7.2 nm. The  $\text{N}_2$ -sorption results show that the abundance of the second desorption step is increasing going from 0.6 to 2 mL, but at higher amounts of TTIP, the second step of the  $\text{N}_2$  isotherms remains unchanged. This means that no extra pore volume is narrowed by the deposition of a higher titania amount. The extra deposited titania can be located outside the pores or inside closing the pore completely, so that this pore is no longer measured with  $\text{N}_2$ -sorption. On the other hand, it is also possible that the second desorption step is in fact increasing, but that this increase is not visible, because the total isotherm is compressed by the fact that isotherms are calculated per gram material ( $\text{SiO}_2 + \text{TiO}_2$ ). So, only based on  $\text{N}_2$ -sorption, it is not possible to completely clarify the structure of the prepared material. Therefore, other experiments were carried out.

Adsorption and photocatalytic degradation of rhodamine 6G have been recorded to investigate whether the position of the nanoparticles, in- or outside the structure, influences the catalytic activity. For all samples the adsorption capacity was measured during 100 min (see Fig. 2a). It is clear that for the low titania loadings (0.6 and 2 mL) it takes 60 min before the adsorption–desorption equilibrium is reached compared to samples with higher loadings (4 mL and higher), where it only takes 20 min. Most likely, it is difficult for the rhodamine 6G molecules to pass the titania nanoparticles inside the SBA-15 channels, causing diffusion limitations in the narrowed pores and slower adsorption–desorption equilibrium. This slower adsorption–desorption equilibrium is also visible in the adsorption kinetics. The adsorption follows a second order reaction kinetic for all samples, shown in Fig. 2b. The second order constant  $k_2$  (in  $\text{g mg}^{-1} \text{min}$ ) was

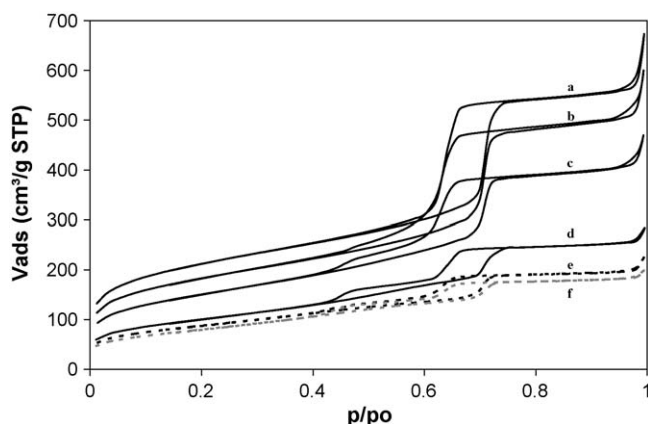


**Fig. 1.**  $\text{N}_2$ -sorption isotherms of (a) initial SBA-15 support, (b) 0.6 mL TTIP, (c) 2 mL TTIP, (d) 4 mL TTIP, (e) 6 mL TTIP and (f) 7.4 mL TTIP.

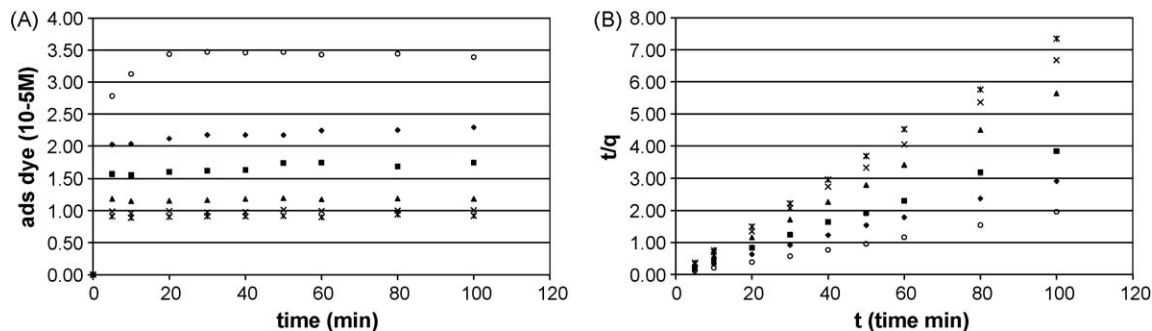


**Fig. 2.** (A) Adsorption and (B) second order kinetics of rhodamine 6G on (○) SBA-15 and SBA-15 loaded with different TTIP amount (◆) 0.6 mL, (■) 2 mL, (▲) 4 mL, (×) 6 mL and (\*) 7.4 mL.

**Table 2**

Second-order constants ( $\text{g mg}^{-1} \text{min}$ ) of the adsorption with rhodamine 6G or methylene blue on the SBA-15 samples with different TTIP amounts.

	R6G	MB
SBA-15	0.0665	0.0156
0.6 mL SBA-15	0.0170	0.0214
2 mL SBA-15	0.0341	0.0121
4 mL SBA-15	0.1765	0.0161
6 mL SBA-15	0.1242	0.0169
7.4 mL SBA-15	0.1468	0.0118

calculated from these curves and can be found in Table 2. The second order constant is low for the samples with long equilibrium time. For higher loadings (4 mL and higher), the large amount of nanoparticles narrows the mesopores to a larger extent so that the rhodamine 6G molecules can not pass them. Therefore, the slow diffusion into the narrowed pores does no longer exist, leading to a fast equilibrium and lower amounts of adsorbed rhodamine 6G. The second-order constant for these samples is remarkably higher than those with slow equilibrium (see Table 2). An adsorption experiment with methylene blue was carried out to evaluate if a smaller dye can still pass the nanoparticles at higher loadings. Fig. 3a shows the adsorption of methylene blue on SBA-15 with different TTIP amounts, it takes long (up to 80 min) before the equilibrium is reached. This is comparable with the adsorption results with rhodamine 6G. However for the samples with TTIP > 4 mL, it also takes 80 min to reach equilibrium, compared to only 20 min with rhodamine 6G. The slow adsorption is also clearly visible in the low second-order values (see Table 2 and Fig. 3b). This slow adsorption indicates again the presence of diffusion limited transport of methylene blue. This means that methylene blue is still able to pass the nanoparticles, due to its smaller dimensions. Based on these results, it can be

concluded that by deposition of 4 mL, the pores become so narrowed that rhodamine 6G can not pass the nanoparticles. However, not all the pores are completely blocked, because methylene blue can still adsorb in the narrowed pore volume. These results show the potential of these materials for e.g. size selective applications. The adsorption of methylene blue proves that more pore volume is narrowed, although no increase in second step desorption was observed with  $\text{N}_2$ -sorption (Fig. 1). The results show that high  $\text{TiO}_2$  amounts strongly influence the  $\text{N}_2$ -sorption results. Therefore, it is important to interpret the  $\text{N}_2$ -sorption results carefully and this for all studies with high amounts of heavy elements deposited on  $\text{SiO}_2$ . In general, for all adsorptions (rhodamine 6G or methylene blue), the adsorption capacity decreases with increasing  $\text{TiO}_2$  loading. This is in good agreement with the decreasing surface area, which was measured with  $\text{N}_2$ -sorption for increasing TTIP amount.

The photocatalytic activities of the samples were measured (Fig. 4). It was expected that the amount of rhodamine 6G removed by photodegradation increases with increasing  $\text{TiO}_2$  content. An increase of the photocatalytic activity was observed going from 0.6 mL to 6 mL, however there exists no linear relationship between the photocatalytic activity and the  $\text{TiO}_2$  amount. If the initial TTIP amount was increased from 0.6 to 2 mL, the photocatalytic activity increases clearly. But when the TTIP amount is further increased to 4 mL, there is only a slight increase in photocatalytic activity. This suggests that the extra amount of deposited anatase is not fully accessible to the rhodamine 6G molecules. Evidence for a disturbed accessibility was already observed in the adsorption experiments, where the rhodamine 6G molecules showed fast adsorption-desorption equilibrium suggesting that some parts of the mesopores are no longer accessible. By depositing 6 mL TTIP, it is expected that the photocatalytic activity would decrease further compared with 4 mL. Nevertheless,

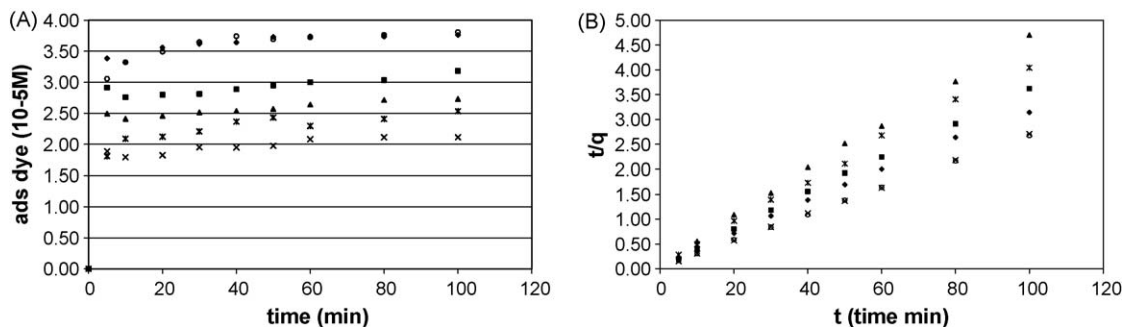


**Fig. 3.** (A) Adsorption and (B) second order kinetics of methylene blue on (○) SBA-15 and SBA-15 loaded with different TTIP amount (◆) 0.6 mL, (■) 2 mL, (▲) 4 mL, (×) 6 mL and (\*) 7.4 mL.



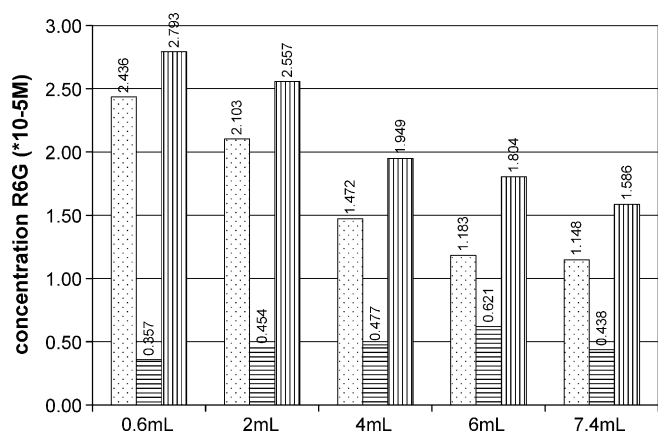


**Fig. 4.** Concentration of rhodamine 6G removed (□) after 30 min adsorption, (▨) after 60 min of photodegradation and (▩) removed in total (adsorption and catalysis) for the different TTIP amounts on SBA-15.

the results show that the photocatalytic activity increases slightly for 6 mL of TTIP, the catalytic activity per weight percentage Ti also increases going from 4 to 6 mL TTIP. This higher photocatalytic activity indicates that the accessibility of the anatase nanoparticles has improved again. This can be due to the different position of the anatase nanoparticles in the formed materials. Based on these results, we assume that for 6 mL TTIP, part of the nanoparticles are located on the outer surface area of the SBA-15 material, in the interparticle space. The decrease in  $N_2$ -sorption at high relative pressures ( $p/p_0 = 0.9–0.99$ ) confirms the filling of interparticle porosity. The anatase particles deposited in the interparticle space are very good accessible, resulting in an increased photocatalytic activity. When the deposited amount of titania is further increased to 7.4 mL, a material with lower photocatalytic activity is obtained. The large amount of particles on the external surface decreases the accessibility of all nanoparticles. Fig. 5 is a hypothetic schematic representation of the materials characteristics and position of the titania nanoparticles at different titania loadings based on the above results. In this scheme, the shaded part of the pores represents the pore volume which rhodamine 6G can not access, because it is too narrow.

To support part of the scheme of Fig. 5, electron tomography is used in order to locate the position of the nanoparticles. Indeed, it is not straightforward to determine the exact location of nanoparticles in a 3D mesoporous network based on only 2D projections as is done in conventional TEM. Therefore, electron tomography was performed. This is a method in which a 3D structure is reconstructed from a series of (S)TEM images acquired at successive tilts. In this case, the images were acquired in

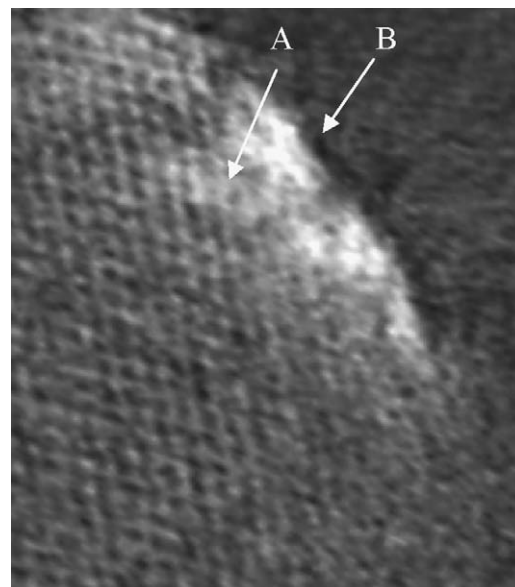


**Fig. 6.** 3D tomography results of 6 mL SBA-15: slice through the reconstruction, whereby A indicates  $TiO_2$  particles inside the mesoporous structure and B  $TiO_2$  particles outside the mesoporous channels.

HAADF-STEM mode at regular tilt intervals of  $2^\circ$ . Due to the limited spacing between the pole pieces in the objective lens of the electron microscope however, only a tilt range of  $-72^\circ$  to  $+64^\circ$  can be sampled. Based on these projections, a 3D reconstruction can be made using an iterative reconstruction scheme (SIRT) [51]. In order to visualize this 3D reconstruction, one can make slices through the structure, displaying an inner section of the structure. Such a 3D reconstruction was not carried out for all materials, but only for SBA-15 6 mL. Fig. 6 shows a slice through the reconstruction. The results show that  $TiO_2$  nanoparticles can be found in (A) but mostly outside (B) the mesoporous channels. A 3D reconstruction of this material can also be found in the supporting information.

For support materials with pore sizes similar to SBA-15, the anatase nanoparticles can be located completely on the inside of the channels (TTIP amount  $< 4$  mL) or they can be located both inside and outside of the mesoporous channels (TTIP amount  $> 6$  mL). The location of these nanoparticles is not only depending on the TTIP amount but also depends on the supporting material used in the synthesis method. Using supporting materials with different porous characteristics can lead to different results after deposition. In this study MCF is used as a second support. It can be seen in Table 1 that MCF has a much higher total pore

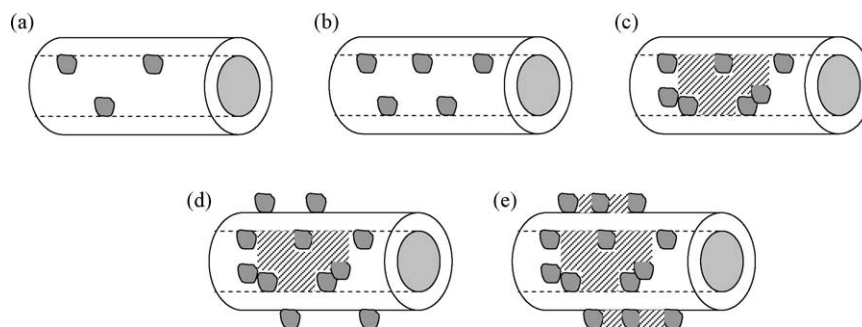


**Fig. 5.** Schematic representation of the materials synthesized with different amounts of TTIP on SBA-15: (a) 0.6 mL, (b) 2 mL, (c) 4 mL, (d) 6 mL and (e) 7.4 mL. Rhodamine 6G can not reach the shaded part. No catalysis is possible on these locations.

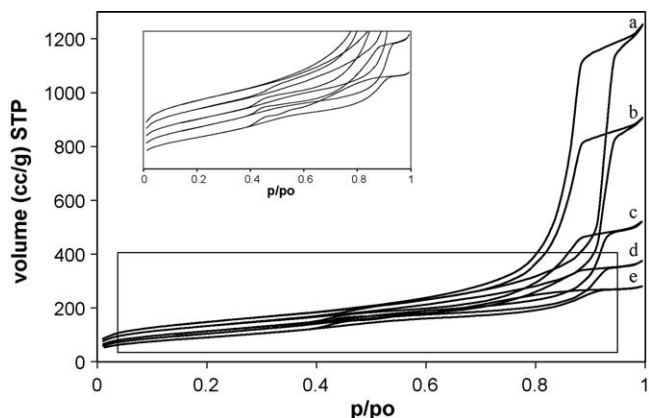


**Fig. 7.**  $N_2$ -sorption isotherms of (a) 0.6 mL MCF, (b) 2 mL MCF, (c) 4 mL MCF, (d) 6 mL MCF and (e) 7.4 mL MCF. The inset is an enlargement to show the two-step desorption, top down 0.6; 2; 4; 6 and 7.4 mL with respectively offsets of 50; 40; 30; 15 and 0.

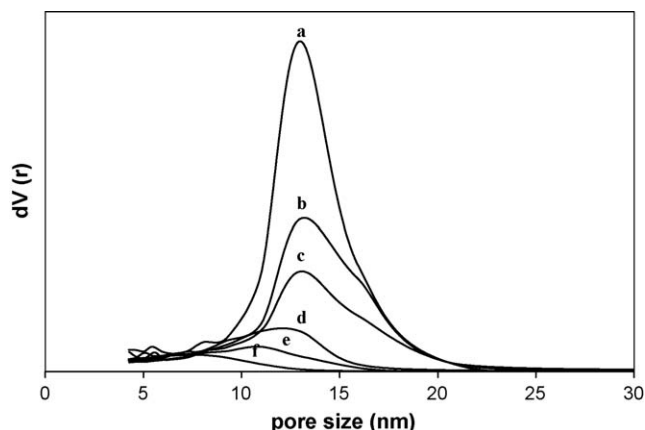


**Fig. 8.** Pore size distribution derived from adsorption curve from (a) MCF, (b) 0.6 mL MCF, (c) 2 mL MCF, (d) 4 mL MCF, (e) 6 mL MCF and (f) 7.4 mL MCF.

volume and average pore diameter than SBA-15. Therefore, it is expected that it will be easier to deposit anatase nanoparticles inside the pores of MCF than in the case of SBA-15. Similar to  $TiO_2$ -activated SBA-15 materials,  $N_2$ -sorption curves of the  $TiO_2$ /MCF materials show a two-step desorption curve. The  $N_2$ -sorption results are shown in Fig. 7. The inset of this figure is an enlargement, making the two-step desorption more visible. This two-step desorption is an indication that the titania particles are indeed situated inside the pores of MCF. All  $TiO_2$  nanoparticles consist of anatase and their size after calcination was calculated as 4.6 nm (similar to the modified SBA-15 materials). Fig. 8 shows the pore size distribution, derived from the adsorption branch, for all these samples. It is deduced that when more than 4 mL of TTIP is added, the pore size decreases to some extent (see also Table 1). But the decrease is the most obvious for 7.4 mL of TTIP. In this case, the pore size is decreased with twice the anatase particle size. This indicates that the deposited anatase nanoparticles have formed a layer inside the MCF channels. To determine the pore diameter and the wall thickness, 2D TEM images of the MCF support and MCF loaded with 7.4 mL TTIP were obtained (see Fig. 9). From these images, the diameter of MCF is found to be  $25.4 \pm 0.2$  nm and the wall thickness equals  $0.7 \pm 0.2$  nm. For MCF loaded with 7.4 mL TTIP, a significant decrease of pore diameter ( $18.6 \pm 0.2$  nm) was observed. This decrease is accompanied by an increase of the wall thickness, which was measured to be  $3.7 \pm 0.2$  nm. These results are in agreement with the  $N_2$ -sorption and XRD results and the hypothesis

that the titania nanoparticles are indeed forming a layer inside the mesopores of the MCF support. Such a shifting of the pore size was not observed for 7.4 mL TTIP deposited on SBA-15. But in case of SBA-15, the particles were located partially inside the pore channels (forming plugs) and partially outside the pore channels (filling up the interparticle space). However MCF has a much larger pore diameter and pore volume so that more particles can be deposited inside the pores. So at higher loadings, all  $TiO_2$  nanoparticles are deposited inside the mesopores forming layers, leading to a lower pore diameter. Similar to the SBA-15 structure, a tilt series for electron tomography was acquired in HAADF-STEM mode, now with a tilt range of  $-74^\circ$  to  $+66^\circ$  and again with intervals of  $2^\circ$ . The result of 6 mL MCF is displayed in Fig. 10 where a slice through the 3D structure is shown so that the inner structure of the material becomes visible. In contrast with 6 mL SBA-15, the 6 mL MCF material only shows  $TiO_2$  particles inside the mesoporous structure and not outside the mesopores. Extra images of the 3D reconstruction of 6 mL MCF are shown in the supporting information. Similar to what was observed on SBA-15, the adsorption capacity of rhodamine 6G decreases with increasing TTIP, due to the decreasing surface area and pore volume. The difference in location of the nanoparticles will influence the catalytic activity of the formed materials. For SBA-15, the photocatalytic activity increased going from 4 to 6 mL of deposited TTIP, because part of the nanoparticles were located outside the pore channels. However, this is not observed for the activated MCF materials (Fig. 11). It is confirmed that the anatase particles are

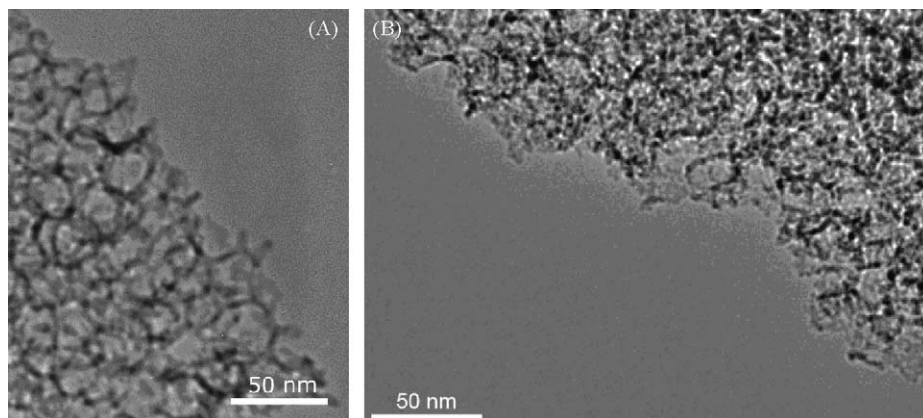


**Fig. 9.** Conventional TEM images of (A) MCF and (B) 7.4 mL MCF.

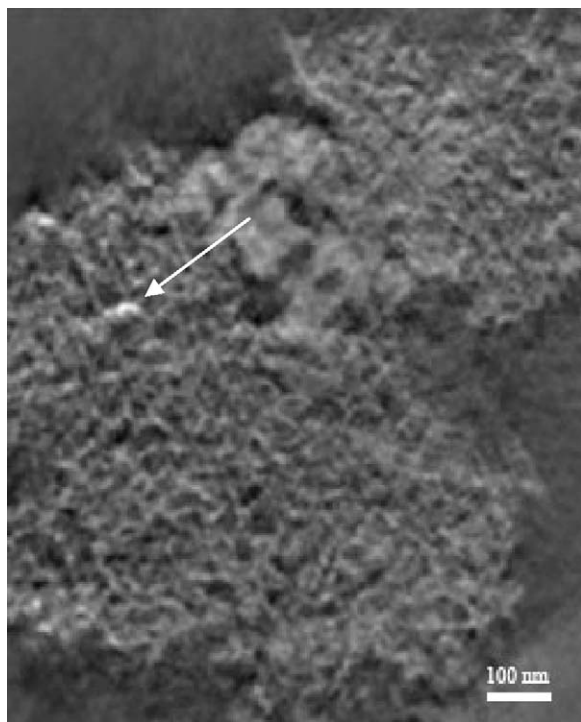


**Fig. 10.** A cross-section of the reconstruction of 6 mL MCF, based on a tilt series recorded in HAADF-STEM mode. The arrow indicates  $\text{TiO}_2$  nanoparticles inside the structure.

located inside the porous structure of MCF. At higher loadings (6 and 7.4 mL) the photocatalytic activity does not improve with increasing titania content. This indicates that the nanoparticles are less accessible. In comparison to SBA-15, MCF suffers from a low accessibility at higher loadings. The low accessibility can be explained by the fact that layer formation is obtained for this sample: the anatase particles are located very close to each other in a way that the rhodamine 6G molecules can not adsorb and react on the complete surface of the anatase nanoparticles.

Since MCF will allow a complete deposition of  $\text{TiO}_2$  nanoparticles on the internal surface, MCF is a better supporting material, when the outer surface of the catalyst needs to be inert. This is important for e.g. textile applications, where anatase may only degrade pollutants and not the colour of the textile.

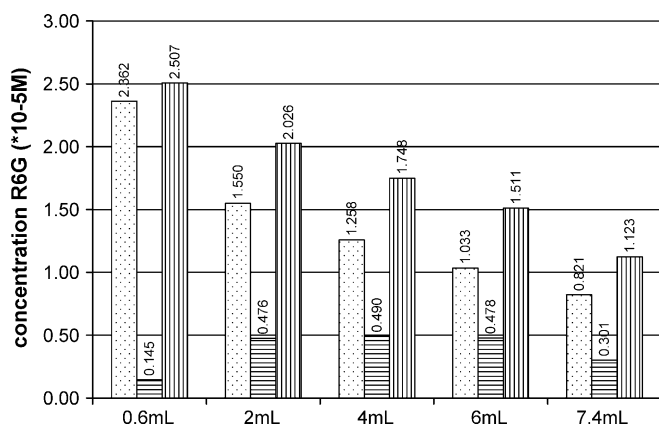


**Fig. 11.** Concentration of rhodamine 6G removed (□) after 30 min adsorption, (▨) after 60 min of photodegradation and (■) removed in total (adsorption and catalysis) for the different TTIP amounts on MCF.

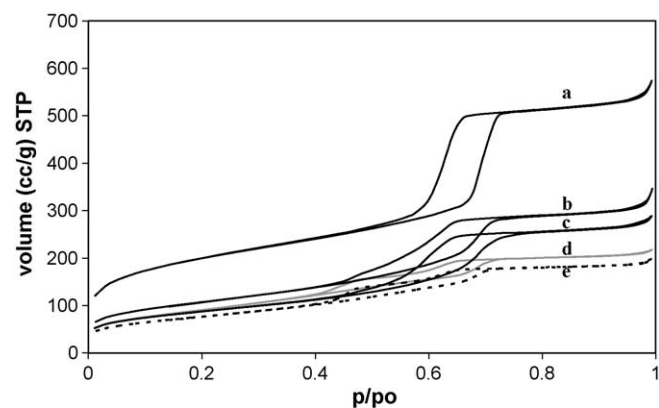


**Fig. 12.**  $\text{N}_2$ -sorption isotherms of (a) initial SBA-15 support, (b) 70/25, (c) 70/70, (d) 25/25 (grey curve) and (e) 25/70 (dotted curve).

### 3.2. The influence of the formation and deposition temperature

The temperature was varied at two different stages during the synthesis procedure. The temperature at which the 7.4 mL TTIP is dissolved in the nitric acid solution (formation temperature) can be altered. Changing this temperature will influence directly the formation of the titania nanoparticles. A second change of temperature is possible at the moment the support is added to the titania solution (deposition temperature). This temperature has a direct impact on the diffusion of the nanoparticles. In the standard synthesis procedure, the formation and deposition of the  $\text{TiO}_2$  nanoparticles are carried out at room temperature (25 °C). For comparison, both these temperatures will be increased to 70 °C. The synthesised samples will be named, *f/d* SBA-15 or *f/d* MCF, where *f* is the formation temperature and *d* is the deposition temperature.

The  $\text{N}_2$ -sorption results for the activated SBA-15 materials are shown in Fig. 12, together with that of the initial support. It can be seen that the shape of the isotherms is completely different, when the formation temperature is increased from room temperature up to 70 °C, independently of the deposition temperature. When the particles are formed at room temperature (Fig. 12d and e), the  $\text{N}_2$ -sorption curves possess only a small condensation step and a clear two-step desorption. In contrast, at 70 °C formation temperature (Fig. 12b and c), the  $\text{N}_2$ -sorption curves show a much larger condensation step, leading to materials with higher pore volumes (see also Table 3). Moreover the two-step desorption is less clear when the particles were formed at 70 °C (especially for the sample

**Table 3**

Structural properties of the samples prepared at different temperatures.

	$S_{\text{BET}}$ ( $\text{m}^2/\text{g}$ ) <sup>a</sup>	$V_{\text{p}}$ ( $\text{cm}^3/\text{g}$ ) <sup>b</sup>	$D_{\text{BJH}}$ (nm) <sup>c</sup>	wt% $\text{TiO}_2$ <sup>d</sup>	Crystal size A/R (nm) <sup>e</sup>
SBA-15	701	0.82	6.8	–	–
25/25 SBA-15	327	0.32	6.8	76	4.5/–
25/70 SBA-15	273	0.29	6.8	77	4.5/–
70/25 SBA-15	383	0.47	6.8	62	5.2/13.7
70/70 SBA-15	313	0.41	6.8	60	5.7/13.8
MCF	611	2.50	26	–	–
25/25 MCF	276	0.34	16	76	3.9/–
25/70 MCF	285	0.38	16	75	4.2/–
70/25 MCF	331	0.73	18	58	5.0/12.4
70/70 MCF	264	0.51	16	73	6.3/12.4

<sup>a</sup>  $S_{\text{BET}}$  is the specific surface area.

<sup>b</sup>  $V_{\text{p}}$  is the total pore volume.

<sup>c</sup>  $D_{\text{BJH}}$  is the pore diameter determined from the adsorption branch using the Barret–Joyner–Halende (BJH) model.

<sup>d</sup> Determined with EPMA.

<sup>e</sup> Crystal size of the anatase(A)/rutile(R) particles calculated from XRD results.



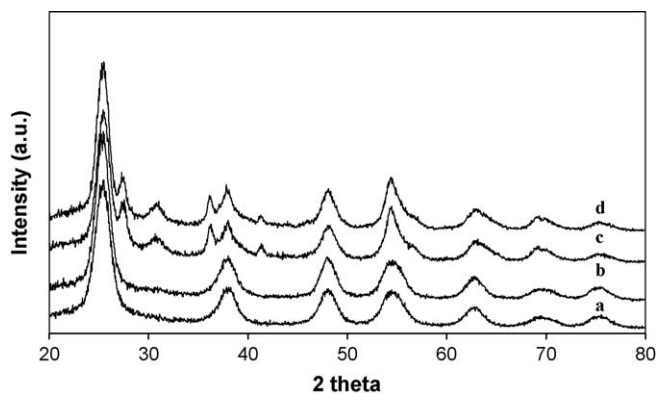


Fig. 13. XRD of the calcined SBA-15 materials synthesized at (a) 25/25, (b) 25/70, (c) 70/25 and (d) 70/70.

70/70). These results suggest that the particles formed at room temperature are small enough to diffuse partially into the SBA-15 channels (resulting in a two-step desorption and a strong decrease of the total pore volume). However, the particles formed at 70 °C did not easily diffuse in the SBA-15 channels. Many particles will be deposited outside the mesopores and have less influence on the porous properties. These materials also have a lower titania content (Table 3), because particles on the outer surface are more easily washed away during the synthesis. The size of the formed nanoparticles was determined from the X-ray diffractograms of the calcined samples (Fig. 13). The nanoparticles formed at room temperature (Fig. 13a and b) only consist of anatase. However, the nanoparticles synthesised at 70 °C (Fig. 13c and d) are a mixture of anatase and rutile. The calculated sizes of the nanoparticles are summarized in Table 3. The obtained rutile crystals are much larger than the anatase crystals. These large rutile crystals (13.7–13.8 nm) are not able to diffuse into the mesopores of SBA-15 (6.8 nm) and they can inhibit anatase crystals to enter the pores. Therefore, all rutile nanoparticles and part of the anatase nanoparticles will be deposited on the outer surface of SBA-15, when the formation temperature is 70 °C. This explains the less pronounced two-step desorption curve and the smaller changes in porosity (compared with the original SBA-15) for the materials with particles formed at 70 °C. For depositions at elevated temperature, the particles have higher kinetic energy and diffuse better inside the porous structure. Chiker et al. observed a more homogeneous dispersion of titanium in SBA-15, when the deposition temperature was increased [52]. In our study,  $N_2$ -sorption results show a higher amount of narrowed pore volume for the sample 25/70 SBA-15 compared with 25/25 SBA-15. This indicates that more particles (formed at room temperature) diffuse inside the pores of SBA-15, when they are deposited at 70 °C. However, when the particles are formed at 70 °C, increasing the deposition temperature does not lead to a better diffusion of the particles inside the pores. After all, an increase of the second desorption step could not be observed for the 70/70 SBA-15 sample compared with the 70/25 SBA-15 samples. So it can be concluded that an elevated deposition temperature only improves the diffusion, when the particles are small enough to fit inside the pores.

All samples were photocatalytically tested and the results are shown in Fig. 14. There are no significant differences in the amount of degraded dye for all samples. However, two remarks must be kept in mind, evaluating the photocatalytic activity. The 70/x samples have 10% less titania in their structures and part of that titania is rutile. Unfortunately, due to the broadness of the XRD peaks, it was not possible to calculate the exact rutile/anatase ratio.

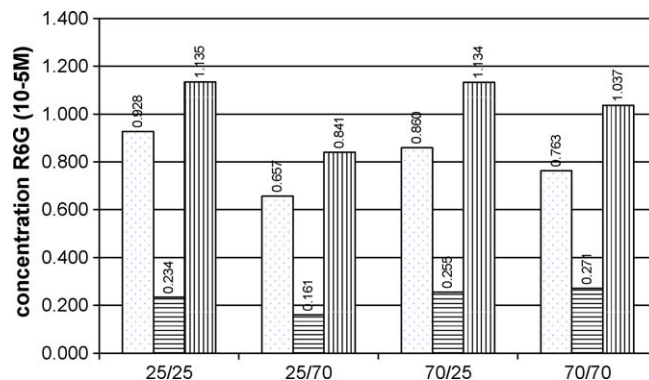


Fig. 14. Concentration of rhodamine 6G removed (□) after 30 min adsorption, (▨) after 60 min of photodegradation and (■) removed in total (adsorption and catalysis) for the different temperatures on SBA-15.

The 70/x samples possess higher catalytic activity per gram of anatase than the 25/x samples. Two reasons are given for this relative higher catalytic activity: (1) When the particles were formed at 70 °C, more anatase particles were located outside the SBA-15 channels compared with the 25/x samples. After all, the large rutile particles (which could not enter the mesopores) can block the pore entrance of the SBA-15 channels. This way, less anatase particles entered the SBA-15 channels. The anatase particles at the outer surface are better accessible than the anatase inside the SBA-15 channels. (2) The anatase particles on the external part of SBA-15 are in close contact with the rutile particles (70 °C formation temperature). It is known that the coexistence of rutile and anatase leads to an increased catalytic activity [53].

Due to the small pores ( $\phi = 6.8$  nm) of SBA-15, the rutile particles formed at 70 °C, prevent part of the other smaller (anatase) particles to enter the SBA-15 channels. But for MCF materials, the pore diameter (26 nm) is much larger, so that it can be expected that even the rutile nanoparticles (12.4 nm) are able to enter the pores. To confirm this, MCF was used as supporting material instead of SBA-15 in the study of the influence of the temperature. The  $N_2$ -sorption results of the obtained materials are shown in Fig. 15. All the synthesised materials possess a two-step desorption curve, but for 70/25 MCF and 70/70 MCF the second step is more pronounced. This indicates that the larger rutile particles could indeed diffuse inside the MCF pores, narrowing the pores. However, the shape of the desorption curve is different, depending on the synthesis conditions. When the particles are formed at room temperature, the second step of the desorption

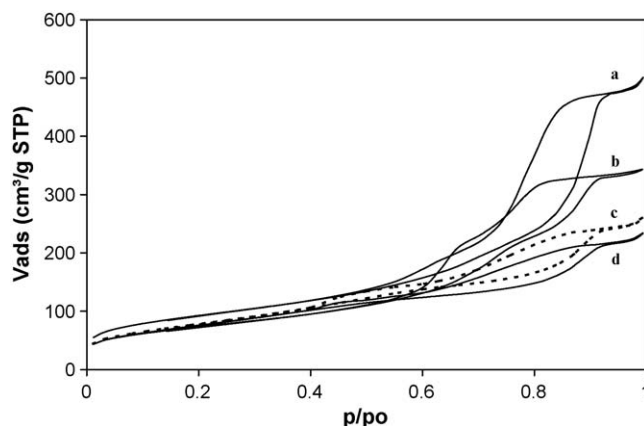
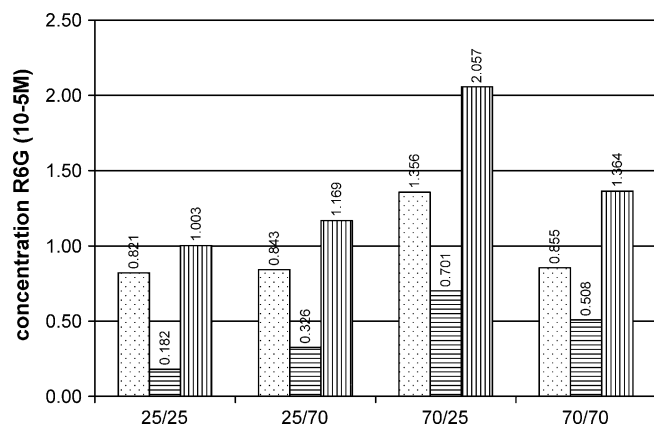


Fig. 15.  $N_2$ -sorption isotherms of (a) 70/25 MCF, (b) 70/70 MCF, (c) 25/70 MCF and (d) 25/25 MCF.



curve is more like a tail rather than a steep step, whereas at 70 °C formation temperature, the second step is situated in a smaller relative pressure range, but with a steeper decrease. This means that although the larger rutile nanoparticles can enter the pores of MCF, deposition of a rutile/anatase mixture (formed at 70 °C) changes the structure in a different, more extreme way than deposition of anatase nanoparticles alone (25 °C). For the 70/x MCF samples even a two-step adsorption was obtained (most visible for 70/70 MCF). The porous characteristics and the titania loadings are summarized in Table 3. The titania content of the MCF 70/25 sample (58 wt%) much lower compared with the other samples, but comparable with 70/25 SBA-15 and 70/70 SBA-15. Probably, the particles formed at 70 °C have a low mobility, but the mobility can be increased by elevation of the deposition temperature. Thereby, more TiO<sub>2</sub> is deposited inside the pores, strongly influencing the porosity of the final material.

The adsorption capacity of these MCF samples, is shown in Fig. 16. The adsorbed amount for 25/25 MCF, 25/70 MCF and 70/70 MCF is similar due to their similar surface area. Only the adsorption capacity of 70/25 MCF, possessing higher porous characteristics, is higher. The prepared samples were catalytically tested for the degradation of rhodamine 6G under UV light. (Fig. 16) In contrast with the SBA-15 analogues, large differences in catalytic activity were obtained for the MCF samples. The photocatalytic activity of the MCF 70/x samples is significantly higher than the MCF 25/x samples. This can be ascribed to the coexistence of rutile and anatase nanoparticles in these materials. In contrast with the analogue SBA-15 samples, the increase in photocatalytic activity is much more pronounced for MCF. A possible explanation for this difference is the fact that for the SBA-15 samples, part of the anatase diffuses in the SBA-15 channels (6.8 nm), whereas rutile can not enter the pores due to its large size (13.7 nm). Therefore, less anatase crystals are in close contact with the rutile nanoparticles. Only the anatase particles, located on the external surface of SBA-15 are in contact with the rutile particles. When MCF is applied as support, the large pores (26 nm) allow diffusion of the rutile particles (12.4 nm) within the pores. Therefore anatase and rutile are both located inside the mesopores being in close contact. Ohno et al. already stated that rutile and anatase have to be in contact with each other to get a synergetic effect on the photocatalytic activity [53]. We can however give no straightforward explanation for the fact that the MCF 70/25 sample, with lower titania content has a higher catalytic activity than MCF 70/70. It is possible that the size of the anatase particles causes (partially)



**Fig. 16.** Concentration of rhodamine 6G removed (□) after 30 min adsorption, (▨) after 60 min of photodegradation and (■) removed in total (adsorption and catalysis) for the different temperatures on MCF.

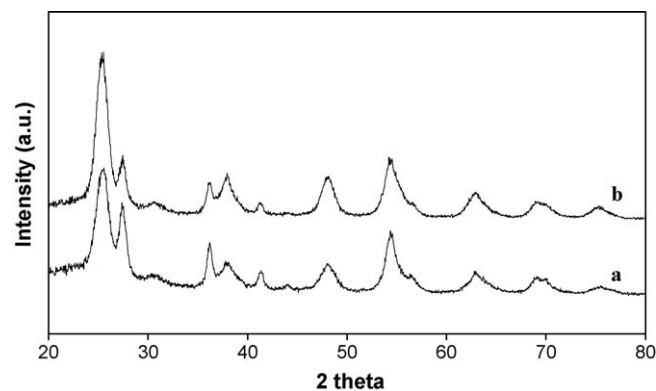


**Fig. 17.** XRD of (a) MCF 70/25 and (b) MCF 70/70 after calcination.

this difference. For MCF 70/25 the anatase particles are about 5 nm whereas for MCF 70/70 the particle size is 6.3 nm. For smaller particles the formed electron-hole pairs can reach the surface more easily, leading to increased catalytic activity [54,55]. Another possibility is that the catalytic difference is a consequence of the different rutile/anatase ratio for these samples. It can be seen from the X-ray diffractograms of the calcined samples (Fig. 17) that MCF 70/25 has a higher rutile/anatase ratio compared with MCF 70/70. However due to the broadness of the peaks, it was not possible to calculate the exact ratio for these samples. It is possible that the rutile/anatase ratio in MCF 70/25 results in an increased photocatalytic activity compared to MCF 70/70. Another possibility is that the TiO<sub>2</sub> nanoparticles are better dispersed (accessible), because of the lower amount (as was observed when different amounts of TTIP were used). However, based on our results, it is not possible to determine which hypothesis is the most plausible one. It could as well be the result of a combination of these different aspects.

#### 4. Conclusion

This study shows that the location and the crystal phase of the titania nanoparticles in a combined TiO<sub>2</sub>/SiO<sub>2</sub> mesoporous photocatalyst can be altered depending on the applied synthesis conditions. This way pre-designed catalysts can be synthesised based on the deposition of TiO<sub>2</sub> nanoparticles obtained by the acid-catalyzed sol-gel method. Both SBA-15 and MCF were used as mesoporous supports. By varying the amount of titanium precursor, the location (inside or outside the mesoporous channels) can be controlled, which strongly influences the photocatalytic activity. The place of deposition also depends on the support. The pore size of the support is very important: using MCF as support allows the deposition of more particles inside the pores. It is possible to introduce 71 wt% TiO<sub>2</sub> inside MCF (confirmed with 3D-tomography), leading to a photocatalyst with inert outer surface. By synthesising the nanoparticles at 70 °C, rutile particles were formed. These rutile particles are larger than the anatase nanoparticles and were too large to diffuse inside the SBA-15 channels. In case the nanoparticles were synthesised at 70 °C, SBA-15 had anatase located inside and outside their pores and rutile positioned only outside, whereby less anatase was in close contact with the rutile particles, having a negative influence on the photocatalytic activity. Due to the large pores of MCF, both anatase and rutile particles were able to diffuse inside the larger mesopores. This way, the rutile and anatase nanoparticles were in close contact with each other leading to increased photocatalytic activity, especially for TiO<sub>2</sub> nanoparticles prepared at 70 °C and deposited on MCF at 25 °C.

## Acknowledgement

This work has been performed within the GOA-BOF program of the University of Antwerpen and within the EU-FP6 NoE project 'Inside Pores'. V. Meynen wants to thank the FWO-Flanders for financial support.

## Appendix A. Supplementary data

Supplementary data associated with this article can be found, in the online version, at [doi:10.1016/j.apcatb.2008.10.009](https://doi.org/10.1016/j.apcatb.2008.10.009).

## References

- [1] R. Van Grieken, J. Aguado, M.J. López-Muñoz, J. Marugán, J. Photoch. Photobio. A 148 (2002) 315–322.
- [2] K. Mogyórosi, J. Németh, I. Dékány, J.H. Fendler, Prog. Colloid Polym. Sci. 117 (2001) 88–93.
- [3] K. Mogyórosi, A. Farkas, I. Dékány, I. Ilisz, A. Dombi, Environ. Sci. Technol. 36 (2002) 3618–3624.
- [4] R. Kun, M. Balázs, I. Dékány, Colloid. Surface. A 265 (2005) 155–162.
- [5] G.J. de, A.A. Soler-Illia, C. Sanchez, B. Lebeau, J. Patarin, Chem. Rev. 102 (2002) 4093–4138.
- [6] P. Yang, D. Zhao, D.I. Margolese, B.F. Chmelka, G.D. Stucky, Nature 396 (1998) 152–155.
- [7] G.J. de, A.A. Soler-Illia, A. Louis, C. Sanchez, Chem. Mater. 14 (2002) 750–759.
- [8] D. Grosso, G.J. de, A.A. Soler-Illia, F. Babonneau, C. Sanchez, P.-A. Albouy, A. Brunet-Bruneau, A.R. Balkenende, Adv. Mater. 13 (2001) 1085–1090.
- [9] K. Cassiers, T. Linssen, V. Meynen, P. Van Der Voort, P. Cool, E.F. Vansant, Chem. Commun. (2003) 1178–1179.
- [10] K. Cassiers, T. Linssen, M. Mathieu, Y.Q. Bai, H.Y. Zhu, P. Cool, E.F. Vansant, J. Phys. Chem. B 108 (2004) 3713–3721.
- [11] E. Beyers, P. Cool, E.F. Vansant, Micropor. Mesopor. Mat. 99 (2007) 112–117.
- [12] D.C.M. Dutoit, M. Schneider, A. Baiker, J. Catal. 153 (1995) 165–176.
- [13] D.C.M. Dutoit, U. Göbel, M. Schneider, A. Baiker, J. Catal. 164 (1996) 433–439.
- [14] S. Cao, K.L. Yeung, P.-L. Yue, Appl. Catal. B - Environ. 65 (2006) 99–108.
- [15] K. Brodzik, J. Walendziewski, M. Stolarski, L. Van Ginneken, K. Elst, V. Meynen, J. Porous Mat. 14 (2007) 219–226.
- [16] N. Yao, S.L. Cao, K.L. Yeung, Micropor. Mesopor. Mat. [Doi:10.1016/j.micromeso.2008.08.020](https://doi.org/10.1016/j.micromeso.2008.08.020).
- [17] S.L. Cao, N. Yao, K.L. Yeung, J. Sol-Gel Sci. Techn. 46 (2008) 323–333.
- [18] S.L. Cao, K.L. Yeung, P.L. Yue, Appl. Catal. B - Environ. 76 (2007) 64–72.
- [19] N. Hüsing, B. Launay, D. Doshi, G. Kickelbick, Chem. Mater. 14 (6) (2002) 2429–2432.
- [20] N. Huesing, B. Launay, G. Kickelbick, S. Gross, L. Armelao, G. Bottaro, M.P. Feth, H. Bertagnolli, G. Kothleitner, Appl. Catal. A - Gen. 254 (2003) 297–310.
- [21] Y. Chen, Y. Huang, J. Xiu, X. Han, X. Bao, Appl. Catal. A - Gen. 273 (2004) 185–191.
- [22] P.V. Messina, M.A. Morini, M.B. Sierra, P.C. Schulz, J. Colloid Interf. Sci. 300 (2006) 270–278.
- [23] X. Zhang, F. Zhang, K.-Y. Chan, Appl. Catal. - Gen. 285 (2005) 119–125.
- [24] X. Zhang, F. Zhang, K.-Y. Chan, Appl. Catal. A - Gen. 284 (2005) 193–198.
- [25] Y. Li, S.-J. Kim, J. Phys. Chem. B 109 (2005) 12309–12315.
- [26] K. De Witte, A.M. Busuioac, V. Meynen, M. Mertens, N. Bilba, G. Van Tendeloo, P. Cool, E.F. Vansant, Micropor. Mesopor. Mat. 110 (2008) 100–110.
- [27] C. Xie, Z. Xu, Q. Yang, B. Xue, Y. Du, J. Zhang, Mat. Sci. Eng. B - Solid 112 (2004) 34–41.
- [28] M.M. Mohamed, T.M. Salama, T. Yamaguchi, Colloid Surface A 207 (2002) 25–32.
- [29] Y. Chen, K. Wang, L. Lou, J. Photochem. Photobio. A 163 (2004) 281–287.
- [30] A. Battacharyya, S. Kawi, M.B. Ray, Catal. Today 98 (2004) 431–439.
- [31] K. Mogyórosi, I. Dékány, J.H. Fendler, Langmuir 19 (2003) 2938–2946.
- [32] L. Liu, P. Dong, R. Liu, Q. Zhou, X. Wang, G. Yi, B. Cheng, J. Colloid Interf. Sci. 288 (2005) 1–5.
- [33] H.-H. Choi, J. Park, R.K. Singh, Appl. Surf. Sci. 240 (2005) 7–12.
- [34] H. Ding, H. Sun, Y. Shan, J. Photochem. Photobio. A 169 (2005) 101–107.
- [35] M.-J. López-Muñoz, R. Van Grieken, J. Aguado, J. Marugán, Catal. Today 101 (2005) 307–314.
- [36] J. Yang, J. Zhang, L. Zhu, S. Chen, Y. Zhang, Y. Tang, Y. Zhu, Y. Li, J. Hazard Mater. 137 (2006) 952–958.
- [37] W. Wang, M. Song, Mater. Res. Bull. 41 (2006) 436–447.
- [38] W. Wang, M. Song, Micropor. Mesopor. Mat. 96 (2006) 255–261.
- [39] S. Perathoner, P. Lazafame, R. Passalacqua, G. Centi, R. Schlögl, D.S. Su, Micropor. Mesopor. Mat. 90 (2006) 347–361.
- [40] M.V. Landau, L. Vradman, X. Wang, L. Titelman, Micropor. Mesopor. Mat. 78 (2005) 117–129.
- [41] K. De Witte, P. Cool, I. De Witte, J. Rao, G. Van Tendeloo, E.F. Vansant, J. Nanosci. Nanotechnol. 7 (2007) 1–5.
- [42] L. Vradman, M.V. Landau, D. Kantorovich, Y. Kolypin, A. Gedanken, Micropor. Mesopor. Mat. 79 (2005) 307–318.
- [43] E. Van Bavel, P. Cool, K. Aerts, E.F. Vansant, J. Phys. Chem. B 108 (2004) 5263–5268.
- [44] P. Schmidt-Winkel, W.W. Lukens, D. Zhao, P. Yang, B.F. Chmelka, G.D. Stucky, J. Am. Chem. Soc. 121 (1999) 254–255.
- [45] P.J. Holliman, B.V. Velasco, I. Butler, M. Wijdekop, D.A. Worsley, Int. J. Photoenergy 2008 (2008) 7, [doi:10.1155/2008/827605](https://doi.org/10.1155/2008/827605).
- [46] P. Van Der Voort, P.I. Ravikovitch, K.P. De Jong, A.V. Neimark, A.H. Janssen, M. Benjelloun, E. Van Bavel, P. Cool, B.M. Weckhuysen, E.F. Vansant, Chem. Commun. (2002) 1010–1011.
- [47] P. Van Der Voort, P.I. Ravikovitch, K.P. De Jong, M. Benjelloun, E. Van Bavel, E.H. Janssen, A.V. Neimark, B.M. Weckhuysen, E.F. Vansant, J. Phys. Chem. B 106 (2002) 5873–5877.
- [48] M. Kruk, M. Jaroniec, S.H. Joo, R. Ryoo, J. Phys. Chem. B 107 (2003) 2205–2213.
- [49] V. Meynen, P. Cool, E.F. Vansant, Micropor. Mesopor. Mat. 104 (2007) 26–38.
- [50] B.D. Cullity, Elements of X-ray Diffraction, Addison-Wesley Publishing Company, 1967.
- [51] P. Gilbert, J. Theor. Biol. 36 (1972) 105.
- [52] F. Chiker, J.Ph. Nogier, F. Launay, J.L. Bonardet, Appl. Catal. A - Gen. 243 (2003) 309–321.
- [53] T. Ohno, K. Sarukawa, K. Tokieda, M. Matsumura, J. Catal. 203 (2001) 82–86.
- [54] L. Zhao, Y. Yu, L. Song, X. Hu, A. Larbot, Appl. Surf. Sci. 239 (2005) 285–291.
- [55] X. Gao, I.E. Wachs, Catal. Today 51 (1999) 233–254.